

Ab – initio Prediction of Mechanical, Electronic, Magnetic and Transport Properties of Bulk and Heterostructure of a Novel Fe-Cr based Full Heusler Chalcogenide

Joydipto Bhattacharya^{1,2}, Rajeev Dutt^{1,2}, Aparna Chakrabarti^{1,2}

¹ Raja Ramanna Centre for Advanced Technology, Indore-452013, India and

² Homi Bhabha National Institute, Training School Complex, Anushakti Nagar, Mumbai-400094, India

Using electronic structure calculations based on density functional theory, we predict and study the structural, mechanical, electronic, magnetic and transport properties of a new full Heusler chalcogenide, namely, Fe₂CrTe, both in bulk and heterostructure form. The system shows a ferromagnetic and half-metallic(HM) like behavior, with a very high (about 95%) spin polarization at the Fermi level, in its cubic phase. Interestingly, under tetragonal distortion, a clear minimum (with almost the same energy as the cubic phase) has also been found, at a c/a value of ~ 1.26 , which, however, shows a ferrimagnetic and fully metallic nature. The compound has been found to be dynamically stable in both the phases against the lattice vibration. The elastic properties indicate that the compound is mechanically stable in both the phases, following the stability criteria of the cubic and tetragonal phases. The elastic parameters unveil the mechanically anisotropic and ductile nature of the alloy system. Due to the HM-like behavior of the cubic phase and keeping in mind the practical aspects, we probe the effect of strain as well as substrate on various physical properties of this alloy. Transmission profile of the Fe₂CrTe/MgO/Fe₂CrTe heterojunction has been calculated to probe it as a magnetic tunneling junction (MTJ) material in both the cubic and tetragonal phases. Considerably large tunneling magnetoresistance ratio (TMR) of $\approx 10^3$ % is observed for the tetragonal phase, which is found to be one order of magnitude larger than that of the cubic phase.

I. INTRODUCTION

Half-metallic (HM) ferromagnets (FM) have become a topic of active research due to their potential for various technological applications. Theoretically, the HMFMs are shown to exhibit 100% spin polarization (SP) at the Fermi level (E_F), with one of the spin channels showing semi-conducting (SC) and the other one possessing metallic nature. In 1983, half-metallicity has been predicted in some half Heusler alloys (HHA), namely, NiMnSb and its isoelectronic compounds, PtMnSb and PdMnSb.¹ Ever since this study has been published in the literature, the field of HM Heusler alloys (HMHA) has attracted immense attention of the researchers, both theoreticians and experimentalists alike. As a result, innumerable studies on half-metallic half as well as full Heusler alloys (FHA) have come to the fore, in order to either understand some fundamental aspects or explore their potential for various applications.^{2–10}

It has been seen in the literature that typically many of the FHAs exhibit metallic nature, while a large number of HHAs are SC in nature. Many works have been carried out to show that the number of valence electrons (n_v) plays a crucial role in defining the electronic as well as magnetic properties of materials. The Slater-Pauling rule established the relation between n_v and the magnetic moment of a transition metal.^{11,12} Further, for Heusler alloys, specifically for Co-based ones, Slater-Pauling behavior has been seen, as reported in the literature.^{13,14} It has been observed that among the FHAs, primarily Co-based alloys show HM behavior with a typical value of valence electrons (n_v) of 26 to 28. As discussed above, searching for a new or novel HMHA, which has high to very high (preferably 100 %) spin polarization at E_F ,

recently become of utmost importance, both from the points of view of fundamental understanding and technological application.^{15–17} To this end, we take a combination of Fe, Cr and Te atoms, yielding a FHA, Fe₂CrTe, with a n_v value of 28. This alloy contains no Co atom, on the other hand, contains a chalcogen atom, Te. In the recent past, chalcogen atoms have been shown to be elements of interest^{18–22}. From our *ab – initio* electronic structure calculations, it turns out that Fe₂CrTe alloy is expected to show a HM-like behavior. The HM properties have been observed to be greatly influenced by defects, surfaces and interfaces. In this context, the study of the effect of strain as well as substrate on various physical properties of a HMHA can be interesting and important from practical application points of view. Hence, we embark upon the same in the present work. We apply uniform isotropic strain and also apply a biaxial strain by putting the cubic alloy on a well-known and lattice-matched SC substrate, namely, MgO.

In one of our recent works, we have probed the possibility of coexistence of half-metallicity and tetragonal (martensite) transition in a series of Ni- and Co-based FM FHAs, including Ni₂MnGa and a few other well-known alloys.⁵ As a martensite phase transition (MPT) indicates occurrence of a shape memory behavior in a magnetic alloy and a HMFMs alloy has the possibility of application in the field of spintronics, studying both these aspects is important. Since typically it has been observed that the MPT and HM behaviors are not seen in the same material, we have dwelled in the study of the same in the past.⁵ We predicted a novel Co-based FHA (Co₂MoGa), which exhibited a tendency of MPT and also a HM-like behavior. Three of the other studied FHAs have shown a very clear local minimum in the energy versus c/a plot, with a range of values of c/a ratio

(~ 1.25 to 1.35). While the clear display of a tetragonal (martensite) phase is well-known and it is well-studied in many of the FHAs^{5,23–27}, the appearance of a minimum at a c/a ratio other than 1, in an otherwise cubic alloy, has seldom been observed.⁵ In this work, we explore the possibility of a tetragonal distortion for the FHA Fe_2CrTe and find that along with a cubic (austenite) phase, a clear minimum is observed for a tetragonal phase with a c/a ratio of ~ 1.26 , leading to a double-minima like structure in the energy versus c/a plot.

For spintronic devices, in recent times, an extensive search for new materials suitable for magnetic tunneling junction (MTJ) is going on.^{28,29} These heterojunctions comprise two FM electrode materials and a non-magnetic insulator or semi-conducting spacer material in between the two electrodes. In these systems, the tunneling magnetoresistance (TMR) is strongly dependent on the relative spin orientations of both the electrodes (parallel or anti-parallel). The TMR ratio has been defined as the difference in conductance of the MTJ in two different magnetic orientations divided by the smaller value. This ratio can in principle (theoretically) be infinitely large if a HMFm material is used as an electrode in the MTJ. In the literature, many studies have been reported where Co-based HMFm alloys have been used. Most of these studies include a thin insulating layer of MgO as the barrier/spacer material and favorable tunneling properties have been observed in these MTJs.^{4,30–33} As Fe_2CrTe is expected to exhibit a HM-like character, we first probe the magnetic properties of the Fe_2CrTe thin film (13 monolayers (ML)) with 5 (7) ML of MgO as a substrate material. We find that the SP at E_F is about 75% (70%), when 5 (7) ML of MgO substrate. We further calculate the transmission properties of the heterojunctions $\text{Fe}_2\text{CrTe}/\text{MgO}/\text{Fe}_2\text{CrTe}$ to understand and explore the potential for MTJ application.

In the next section, we discuss the method of electronic structure calculations, which is based on density functional theory. We also briefly discuss the calculational method related to transport properties. In the section followed by methodology, we present our results and discuss the same. Finally, we summarize and conclude our work in the last section.

II. METHOD

The FHAs are known to exist either in a conventional or an inverse Heusler alloy structure. From the structure optimization, we find that in the lowest energy state, Fe_2CrTe alloy possesses the conventional structure with a $L2_1$ phase that consists of four interpenetrating face-centered-cubic (fcc) sub-lattices with origin at the following fractional positions: Fe atom at $(0.25, 0.25, 0.25)$ and $(0.75, 0.75, 0.75)$ sites, Cr atom at $(0.5, 0.5, 0.5)$ site and Te atom at $(0, 0, 0)$ site. The structure has been optimized by doing full geometry optimization using Vienna Ab Initio Simulation Package

(VASP)^{34,35} with the projector augmented wave (PAW) method.^{34,35} For exchange-correlation (XC) functional, generalized gradient approximation (GGA) over the local density approximation has been used.³⁶ We use an energy cutoff of 500 eV for the planewaves. The final energies have been calculated with a k mesh of $15 \times 15 \times 15$ for the cubic symmetry and an equivalent number of k -points for the tetragonal symmetry. The energy and force tolerance for our calculations were 1 μeV and 20 $\text{meV}/\text{\AA}$, respectively. For obtaining the electronic properties, the Brillouin zone integration has been carried out using the tetrahedron method with Blöchl corrections. The directional dependencies of different mechanical properties (Young's modulus, inverse of bulk modulus or compressibility, shear modulus, and Poisson's ratio) of this alloy in both the cubic and tetragonal phases have been calculated with the help of the ELATE software.³⁷ For the calculation of transport properties of the heterojunction of Fe_2CrTe and MgO, we make use of the PWCOND code³⁸, which has been implemented in the Quantum ESPRESSO (QE) package³⁹. The spin-dependent tunneling conductance has been calculated using the Landauer formula:

$$G^\sigma = \frac{e^2}{h} \sum_{K_{||}} T^\sigma(K_{||}, E)$$

here $\sigma(\uparrow, \downarrow)$ is the spin index and $T^\sigma(K_{||}, E)$ is the spin-dependent transmission coefficient at a particular energy value E , with $K_{||} = (K_x, K_y)$, where K are the wave-vectors, x and y are directions.

In the literature, Choi and Ihm⁴⁰ have given a method to calculate $T^\sigma(K_{||}, E)$. We perform this calculation for the optimized geometry using the GGA exchange functional.³⁶ We have taken the cut-off energy for the wave function and the charge density as 60 and 600 Ry, respectively. A mesh of $12 \times 12 \times 1$ k -points have been used for the self-consistent-field(SCF) calculation of $\text{Fe}_2\text{CrTe}/\text{MgO}/\text{Fe}_2\text{CrTe}$ heterojunction. A high tolerance (10^{-8} Ry) and a large k -mesh (100 points in both x and y directions) have been taken, which are required to capture the fine spikes in a transmission.⁴¹ The scalar relativistic ultrasoft pseudopotentials(USPP) with the GGA exchange-correlation term have been used, as obtained from the PSLibrary 1.0.0. For further details of calculation of ballistic conductance see Ref.⁴⁰. Convergence of all the relevant parameters for VASP and QE packages have been tested before embarking upon the calculations of the physical properties.

III. RESULTS AND DISCUSSION

In this section, first we predict the energetic stability of the cubic phase of Fe_2CrTe alloy and then explore the possibility of a stable tetragonal (martensite) phase of this alloy, where the c/a ratio (a and c being the lattice constants along the x and z -directions) has been varied, keeping the volume fixed. We then calculate and present

the dynamical and mechanical properties of these two phases. The mechanical properties of the well-known HA Ni_2MnGa have been discussed in some places, for the sake of comparison. Further, we discuss the electronic and magnetic properties of the cubic and tetragonal phases. Due to the near HM behavior of the cubic phase, keeping in mind the practical aspects, we probe this phase further. An important aspect in materials growth is strain. Hence, we simulate and discuss the effect of isotropic strain on the electronic and magnetic properties of cubic Fe_2CrTe alloy. Further, to check the effect of substrate (leading to bi-axial strain), we calculate the physical properties of the thin film (having 13 ML) of the cubic Fe_2CrTe alloy, supported by a suitably lattice-matched substrate MgO (probed both 5 and 7 ML). Finally, the reasonably high SP at E_F (75%) of the alloy when interfaced with MgO motivated us to perform the calculation of transmission properties of the $\text{Fe}_2\text{CrTe}/\text{MgO}/\text{Fe}_2\text{CrTe}$ heterojunctions. We discuss and analyze the results of this heterojunction to probe its MTJ properties.

III.1. Bulk Physical Properties

III.1.1. Energetic and Dynamical Stability

Energetics - The binding energy (BE) of the cubic phase of Fe_2CrTe has been found to be -4.0252 eV per atom (for Ni_2MnGa the BE is -4.3963 eV per atom) and this indicates a stable alloy. As discussed above, the Fe_2CrTe alloy exhibits a lowest energy state in the conventional cubic Heusler alloy structure (Figure 1(a)), like the well-known Ni_2MnGa compound, and it has a lattice constant of 5.95 Å. In order to assess if a stable tetragonal (martensite) phase is possible in this system or not, we vary the c/a value, by keeping the volume same as the cubic phase, since MPT is known to be a volume conserving transition. In Figure 1(b) we show a schematic figure of the tetragonal phase with the optimized c/a ratio of ~ 1.26 . In Figure 1(c), we plot the energy difference between the cubic and tetragonally distorted phase as a function of c/a . We find that the cubic (austenite) phase is very close to the energy of the tetragonal (martensite) phase (lowest energy state) showing a double-minima like plot and the energy difference is as small as ~ 1 meV per atom. In order to cross-check this interesting observation, we carry out an all-electron calculation employing WIEN2k programme package⁴² using the GGA XC term. A plot with a double-minima structure is found in this case too. We find that the energy trend is reversed but the energy difference between the two phases continues to be very small (~ 12 meV per atom). Similar observation of a reversal of energy ordering for very small energy difference between two phases obtained from an all-electron and a pseudopotential calculation has already been reported in the literature.⁴³ Since the energy difference (between the cubic and the tetragonal phases) is very small and the difference between the physical properties, such

as total magnetic moment and density of states (DOS) are insignificant, when results from both the methods are compared, in this work, we continue to consider and present the results of physical properties, obtained from VASP.^{34,35}

In order to understand the energetics further and to probe the possibility of MPT, we calculate the Gibbs free energy for both the cubic and tetragonal states as a function of temperature (Figure 1(d)). Our results show that interestingly, there is no crossing of the curves, which indicates that no MPT is possible in this alloy. This would bring us to the conjecture that since the two phases are energetically rather close and no MPT seems feasible, both these phases will compete and will have equal possibility to form, depending upon the growth conditions. During growth, possibility of finding a material in two (or more) different symmetries has already been discussed by us in our group and the experimental references therein.⁷ However, it may be noted from Figure 1(d) that, at higher temperatures, cubic phase has a slight edge over the tetragonal phase.

Lattice Dynamical Stability - To probe this, we calculate the phonon dispersion curve for the cubic and tetragonal phases and the results are presented in Figure 2. For the phonon calculations, a $4 \times 4 \times 4$ supercell is taken. The finite displacement method within the phonopy code⁴⁴ has been employed in order to obtain the phonon dispersion of the material. From Figure 2 it can be clearly seen that, all the frequencies are positive for both the phases, which is an important prerequisite for the lattice dynamical stability of a material. If the phonon spectra of Fe_2CrTe are compared with other previously studied FHAs^{45,46}, instability in their respective cubic phases are observed. These instabilities are led by the anomalous behavior of the acoustic TA2 branch along the Γ to X direction. However, in the present case, we do not observe clear anomalous dips in the acoustic TA2 branch in the cubic phase (Figure 2). In the cubic phase, along the Γ to X direction, the TA1 and TA2 branches are found to be degenerate and the degeneracy is lifted in the tetragonal phase. The atom projected vibrational density of states (VDOS) for the cubic and tetragonal phases (shown in Figure 2 (a) and (b)) are consistent with our discussion on the phonon spectra. As expected the Te atoms dominate the vibration at lower frequency range, whereas at the higher frequency range, Cr atoms dominate the vibration for both the phases. Hence, in Fe_2CrTe , in both the phases, the sequence of the optical vibration is regular, i.e. decreasing as the mass of the atom is increasing. This behavior is quite different from some other well-known FHAs, which show instability in the cubic (austenite) phase. In those systems, VDOS show unexpected anomalous behavior in the cubic phase, where optical vibration of the lighter atom is seen lying below the optical vibration of the heavier atom.^{45,46} These observations collectively indicate that Fe_2CrTe is stable in both the phases, which gets further support from the variation of the Gibbs free energy with

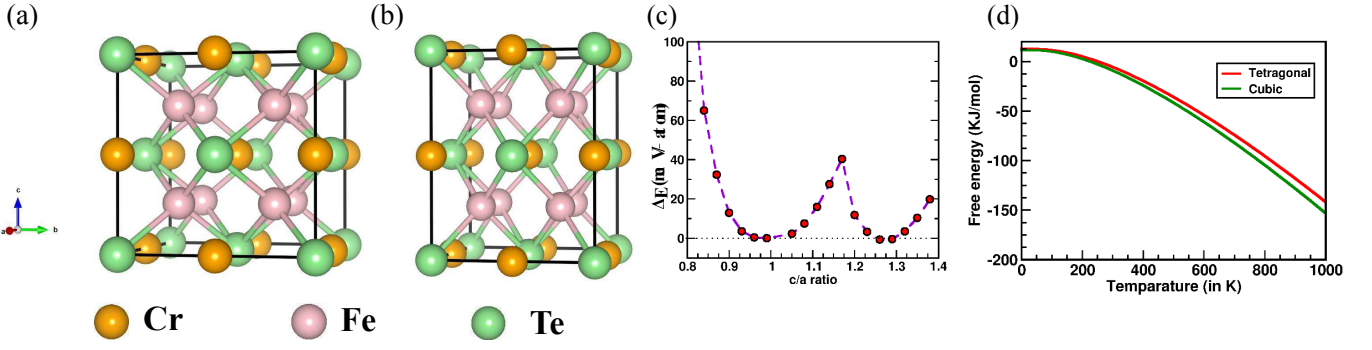


Figure 1. Bulk crystal structure shown in (a) cubic and (b) tetragonal phase. (c) shows the difference in total energy (between cubic and tetragonal phases) with respect to c/a ratio for bulk Fe_2CrTe , where the energy for the bulk cubic phase has been taken as reference. Since we normalize the difference with respect to the energy of the cubic phase, the cubic phase ($c/a = 1$) corresponds to an energy value of 0 eV. (d) Shows the temperature dependent Gibbs free energy, for the cubic and tetragonal phases.

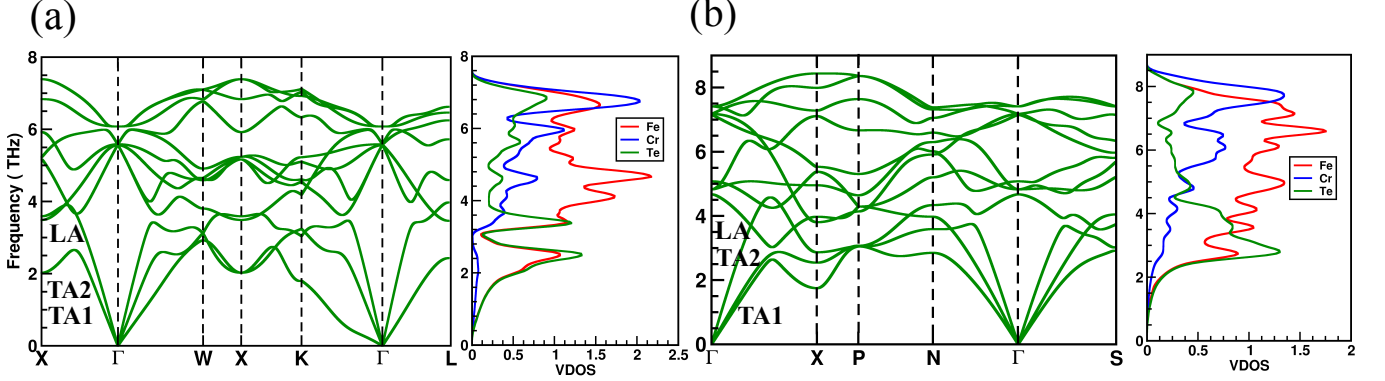


Figure 2. Schematic representation of phonon dispersion relations and atom projected vibrational density of states (VDOS) of (a) cubic and (b) tetragonal unit cell. LA, TA1 and TA2 represent the longitudinal and transverse acoustic branches, respectively.

temperature in these two phases, as discussed before.

III.1.2. Mechanical Properties

Having discussed the stability of the alloy, we now proceed to present and discuss the mechanical properties. For the details of the mathematical expressions for all the elastic constants and parameters, we refer to our earlier work⁴⁷ and the references therein.

In order to study the mechanical stability criteria, we calculate the elastic constants for Fe_2CrTe alloy in cubic phase. It is well-known that there are only three independent ones as $C_{11} = C_{22} = C_{33}$, $C_{12} = C_{13} = C_{23}$ and $C_{44} = C_{55} = C_{66}$ in the cubic phase. We list the three constants C_{11} , C_{12} and C_{44} in Table I. It is well-known that if a cubic system fulfills the following stability criteria, then the structure is mechanically stable.⁴⁹

$$C_{11} - C_{12} > 0 ; C_{11} + 2C_{12} > 0 ; C_{11} > C_{44} > 0$$

In case of Fe_2CrTe , from the results presented in Table I, we find that all the above-mentioned criteria are satisfied, suggesting that it is a mechanically stable alloy in the cubic phase. Further, we calculate the tetragonal shear constant (C') and the Zener ratio (or the elastic anisotropy parameter: A_e) which are defined as:

$$C' = (C_{11} - C_{12})/2$$

$$A_e = \frac{2 \times C_{44}}{C_{11} - C_{12}}$$

We find that while C' has a value of ~ 13 , A_e possesses a value of ~ 8 . It has been established in the literature that a negative or very small positive value of C' indicates an unstable cubic phase, as has been observed for Ni_2MnGa (a value close to 5 has been obtained both from experiments and theory)^{47,50} which has a non-cubic ground state.²⁴ The calculated value for Fe_2CrTe alloy can be considered to be somewhat small, as it has been seen that the typical HM systems like Co_2VGa ⁵¹, which exhibit cubic ground state, show much higher C' values.⁵

Table I. Calculated values of elastic constants (C_{ij} in GPa) for Fe_2CrTe in cubic and tetragonal phases. Computed values of bulk modulus (B in GPa), Young's modulus (E in GPa), Shear modulus (G in GPa), Poisson's Ratio (σ), Cauchy pressure (C_P in GPa) are also tabulated. B and G are calculated using the formalism given by Hill.⁴⁸

Phase	C_{11}	C_{12}	C_{13}	C_{33}	C_{44}	C_{66}	C'	B	E	G	σ	C_P
Cubic	208.86	182.96	-	-	102.89	-	13	191.60	130.52	47.07	0.38	80.10
Tetragonal	330.830	82.493	136.696	271.440	93.966	72.366	124.17	182.76	228.63	88.51	0.29	-11.50

Further, we find that the A_e value turns out to be much larger than 1. It is well-known that materials with an A_e value much different from 1 often shows the tendency to deviate from the cubic symmetry and may suggest instability in the cubic phase.⁵² Presence of a minimum in energy for a tetragonal symmetry (Figure 1(c)) seems to be consistent with the low positive C' and large A_e values corresponding to the cubic bulk phase of Fe_2CrTe alloy.

Now we discuss the mechanical properties, which are important and most-discussed in the literature, namely, the bulk and shear moduli, Young's modulus (E) and Poisson's ratio (σ), which are often used to describe the ductility, malleability and overall mechanical stability of a material. Table I presents these values (all the values being rounded off up to second decimal place). For the cubic phase, we find that the values of bulk, shear and Young's moduli are somewhat higher than those of Ni_2MnGa .^{47,50} This result suggests that in case of tensile, volumetric and shear strains, the present alloy is slightly less compressible compared to Ni_2MnGa . In other words, it is expected to provide larger deformation resistance. However, since the σ value is very close to that of Ni_2MnGa as well as many of the metals, Fe_2CrTe is expected to behave similar to the common metals and well-known HAs in terms of compressibility. A similar conclusion can be drawn from the calculated Pugh's ratio (B/G), which has been found to be ~ 2.77 . On an empirical level, a material with a value higher than the critical value of 1.75 can be considered to have less inherent crystalline brittleness (ICB).⁵³ Further, according to Pettifor⁵⁴, a metal typically exhibits a high positive value of Cauchy pressure. With a value of ~ 80 , which is higher than that of Ni_2MnGa ⁴⁷, more metallic than directional bonding is expected in case of Fe_2CrTe alloy. The Kleinman parameter (ζ) is a dimensionless parameter which corresponds to the relative ease of bond bending to that of bond stretching^{55,56}. Under given stress, bond stretching (bending) dominates if ζ is closer to 0.0 (1.0). We find a value close to 1. Hence, bond lengths are expected to be largely unchanged if the system is distorted.

Next we analyze the elastic stability and mechanical properties of the tetragonal phase. Table I also lists the relevant parameters for the tetragonal phase. The mechanical stability of tetragonal materials correspond to the following conditions: (1) all of C_{11} , C_{33} , C_{44} , $C_{66} > 0$; (2) $(C_{11} - C_{12}) > 0$; (3) $(C_{11} + C_{33} - 2C_{13}) > 0$; (4) $(2(C_{11} + C_{12}) + C_{33} + 4C_{13}) > 0$.⁴⁹ We find all the criteria are fulfilled and hence the tetragonal phase of the

material is mechanically stable. C' value is high and positive, indicating a stable tetragonal phase is possible from the mechanical point of view. However, larger resistance to deformation is indicated by the increased values of B , G and E , compared to the cubic phase. Though the B/G value exhibits similar value as the cubic phase, the C_P value becomes negative, indicating the presence of a less metallic and more directional bonding in the tetragonal phase.

Anisotropic character of mechanical properties - It is well-known that if the value of A_e is 1, the Young's modulus turns out to be isotropic in nature. As we obtain an A_e value much larger than 1, we calculate the maximum and minimum values as well as study the three-dimensional characters to probe the direction-dependent nature of various mechanical properties, including the Young's modulus. Table II gives the maximum and minimum values of Young's modulus (E), compressibility (β), shear modulus (G) and Poisson's ratio (σ). We find that except β , maximum and minimum values for rest of the parameters differ from each other. Further, we probe the directional mechanical properties in two (2D) and three (3D) dimensions. The results (presented in Figures S1 and S2⁵⁷ for cubic and tetragonal phases, respectively) establish the anisotropic nature, more for cubic phase.

III.1.3. Electronic and Magnetic Properties

DOS and Band Structure - In Figure 3, we plot the density of states (DOS) and the band structures of the cubic phase. From the total density of states, we find that there is a high SP at E_F . It is found to be about 95%. The E_F for the equilibrium lattice constant is found to be located on the valence band edge. The majority spin DOS in the occupied region near E_F has dominant contribution from the Cr and Fe d states, with a small contribution from the Te atoms (Figure 3(b)). On the contrary, in case of the minority spin, Fe DOS contributes much more near and at the E_F than the other atoms. These Fe d states in the minority spin channel leads to the reduction of the SP at E_F from 100 to 95%. Further, the unoccupied states in the conduction bands near E_F also has dominant Fe-d character. The orbital projected band structure of Fe_2CrTe in the cubic phase is shown in Figure 3(a), (c). The Δ_1 symmetry is associated with the s , p_x , d_{z^2} orbital character. In contrast, p_x , p_y , d_{xz} , d_{yz} orbitals specify Δ_5 symmetry and d_{xy} , $d_{x^2-y^2}$ orbitals are

Table II. Maximum and minimum values of E (in GPa), β (in TPa^{-1}), G (in GPa) and σ for cubic and tetragonal phases of bulk Fe_2CrTe alloy.

Phase	E		β		σ		G	
	Max	Min	Max	Min	Max	Min	Max	Min
Cubic	261.742	37.994	1.740	1.740	1.301	-0.485	102.891	12.950
Tetragonal	264.527	181.023	1.870	1.801	0.477	0.052	124.168	69.220

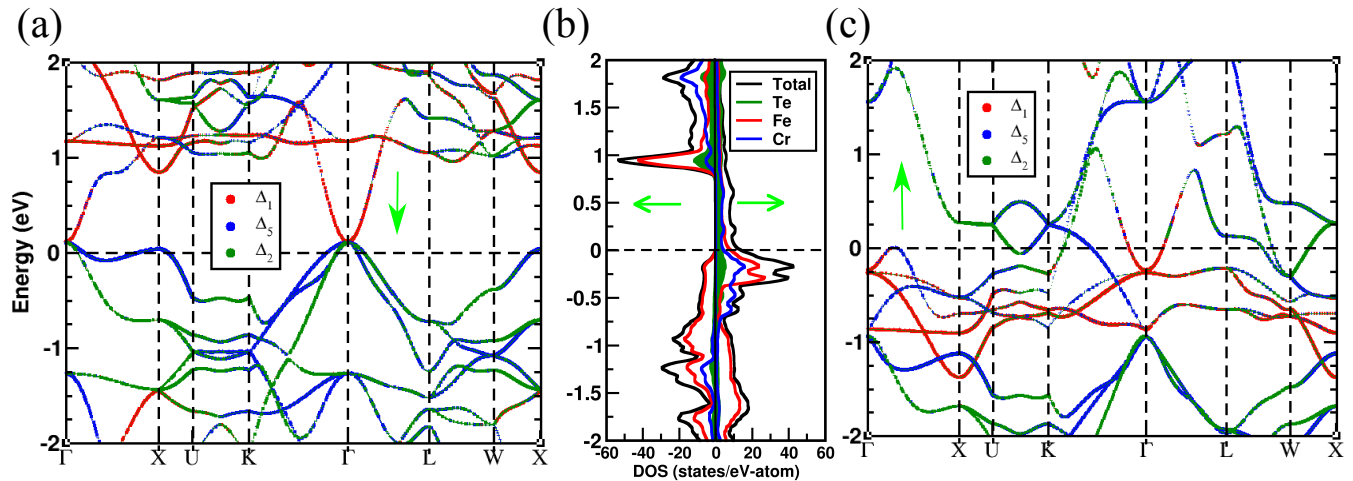


Figure 3. Bulk electronic structure of cubic Fe_2CrTe : (a) and (c) depict orbital projected band structure of minority and majority electrons and (b) gives atom projected density of states. Here $\Delta_1(s, p_z, d_{z^2})$, $\Delta_2(d_{xy}, d_{x^2-y^2})$ and $\Delta_5(p_x, p_y, d_{xz}, d_{yz})$ represent the orbital symmetries of the bands.

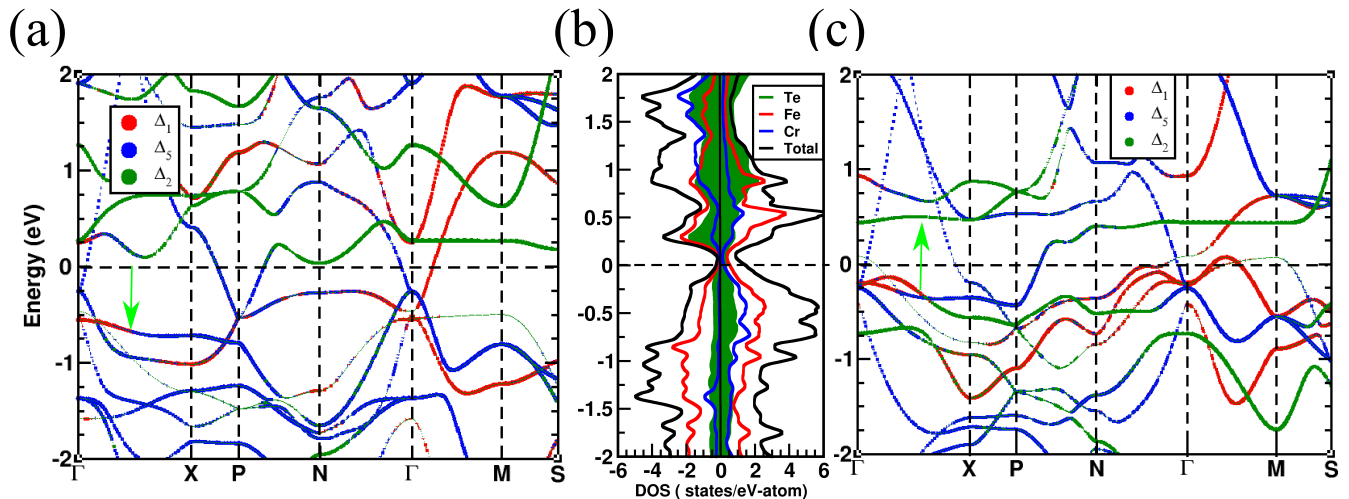


Figure 4. Bulk electronic structure of tetragonal Fe_2CrTe : (a) and (c) show orbital projected band structure of minority and majority electrons and (b) presents atom projected density of states. Here $\Delta_1(s, p_z, d_{z^2})$, $\Delta_2(d_{xy}, d_{x^2-y^2})$ and $\Delta_5(p_x, p_y, d_{xz}, d_{yz})$ represent the orbital symmetries of the bands.

assigned to the Δ_2 symmetry. We can see the presence of highly dispersive parabolic electron like conduction band in the both majority and minority spin channels around the Γ point and these bands have dominant contribution from Δ_1 symmetric bands, originating from Te

5s states. However, we do not observe any bands crossing the E_F along the Γ to X (*i.e.* along $\langle 001 \rangle$) direction in the majority spin channel (Figure 3(c)), which has a great importance in the spin dependent transport properties and we discuss it in the later part of our pa-

per. However, in the minority spin channel, we find two bands cross the E_F , which have dominant Δ_5 and Δ_2 orbital symmetries. Further, in the minority spin case the top of the valence band just touches the E_F , leading to negligible DOS at E_F .

In case of the tetragonal phase (Figure 4), while the majority DOS contributions near the F_F remain similar (both from Fe and Cr d states), the minority DOS at (and also above) E_F gets slightly populated by both Fe and Cr d states, Fe states having more contribution. Due to the increased DOS at E_F for the minority channel, the SP at E_F gets reduced significantly (67%). Other than at the E_F , overall DOS of the tetragonal phase for the majority and minority spin channels also show that the peak positions are rather close to each other unlike the cubic case. This leads to a much lower magnetic moment for the former phase. Further, the orbital projected band structure in Figure 4(a), (c) suggests that parabolic conduction and valence bands around the Γ point in the minority spin channel is pushed away from the E_F and move towards the higher (lower) energy side for the conduction (valence) bands when compared to the cubic case. From the symmetry analyses, we confirm the presence of Δ_1 symmetric band along the Γ - M direction (*i.e.* along the $\langle 001 \rangle$ direction), in both the spin channels. We have further found that there are spaghetti of bands around the high symmetry point Γ in both the spin channels, increasing the valley degeneracy at Γ .

Figure 5 shows the DOS contribution of the various d states of the transition metal elements (Fe and Cr) as these populate the DOS near and at E_F . The splitting of the e_g and t_{2g} like states in the cubic case, specifically in case of Cr, which is in an octahedral symmetry, being surrounded by Fe atoms, is clearly visible from Figure 5 (bottom panel). Although the Fe atoms are the 2nd nearest neighbor of other Fe atoms, the hybridization between them is qualitatively more important. The t_{2g} and e_g like states for Fe atoms, which is in a tetrahedral symmetry, due to the four transition metal atoms Cr as neighbor can be seen from Figure 5 (middle panel). This aspect of crystal-field splitting of the t_{2g} and e_g like states has been shown to play an important role in yielding a HM like behavior in cubic half and full Heusler alloys.^{7,13} The DOS of Cr atom shows much larger energy gap (*i.e.* larger t_{2g} and e_g splitting) around the E_F , larger than what has been observed for Fe_2CrTe bulk (Figure 5 (top panel)). However, the real gap is determined by the Fe-Fe interaction and the t_{2g} , e_g splitting of the Fe atoms. On the contrary, for the case of tetragonal symmetry, due to the absence of clear octahedral/tetrahedral symmetric geometrical environment for the magnetic elements, and consequent absence of crystal-field effect, the splitting between t_{2g} and e_g like states is not clear (Figure 5 (b)). This might have led to the smaller SP value at E_F as compared to the cubic case.

Effect of Hubbard U term - We have also addressed the role of onsite Coulomb interaction (Hubbard U) on the electronic and magnetic properties of Fe_2CrTe in both

the phases. The electron - electron Coulomb interaction and the self-interaction correction are considered in the rotationally invariant way (GGA+U) according to the Dudarev's method⁵⁸. We have considered the U value of Fe and Cr to be 3 eV and 2 eV, respectively. This is in accordance with previous studies reported in the literature.⁵⁹⁻⁶¹. The results are found to be significantly different for both the phases. In the cubic phase the SP at E_F is found to be changed drastically with the Hubbard U parameter (Table S1).⁵⁷ Further analyses on atom-projected DOS indicate that electronic and magnetic properties show significant dependence on U_{Fe} and minimal dependence on U_{Cr} (Figure S3).⁵⁷ However, the SP value in the tetragonal phase shows moderate change over the range of U_{Fe} and U_{Cr} values, considered in our calculation (Table S1).⁵⁷ and the electronic structure is found to be less affected as compared to the cubic phase (Figure S3).⁵⁷ Usually the strength of Hubbard U for each atom in different local environments can be easily estimated by seeking a good agreement between the calculated and the experimental results. However, due to the predictive nature of the present work, the present results await experimental validation.

Fermi Surface - We present the results of calculated Fermi surfaces (FS) for the cubic and tetragonal phases of Fe_2CrTe alloy, for both majority and minority electrons in Figure 6. Further, bands with the respective band indices are shown in Figures S6 and S7⁵⁷, whereas Figure.S5 shows the positions of the high symmetry k-points in the irreducible Brillouin zone.⁵⁷ By analyzing these figures, we observe the following for the cubic phase. The minority spin channel has three bands, 19, 20 and 21, which are mostly Fe derived (small contributions from the Te atoms) and cross E_F . While the former two bands give rise to only a carrier pocket at the Γ point, band number 21 additionally shows a pocket at the X point. On the other hand, in the majority spin channel the bands, 25, 26 and 27 are mostly Cr derived and have small contributions from Fe and Te atoms, specially for band 26. The FS due to band 26 forms a open spherical cone, indicating an electron-like behavior, whereas the FS is hole-like for band 25. Apart from that, small electron-like pockets are also observed at the W point, due to band 27.

In the tetragonal phase, the character of the minority FS is shared by both Fe d and Cr d electrons (see Figure 4). The minority spins generate very small electron-like pockets at the X point and hole-like pockets at the Γ point. But the majority spin FS undergoes significant changes as we go from cubic to tetragonal phase. The majority FS due to band 25, produces small electron-like pockets at the high symmetry points X and N. Large hole-like pockets, centered around the Γ point, can be seen due to band 24. This drastic change in the majority spin FS (as we go from cubic to tetragonal phase) is also accompanied by a change in the spin magnetic moment, as seen for the Fe atoms, which we will discuss in the next section.

Magnetic Properties - As it is clear from Table III,

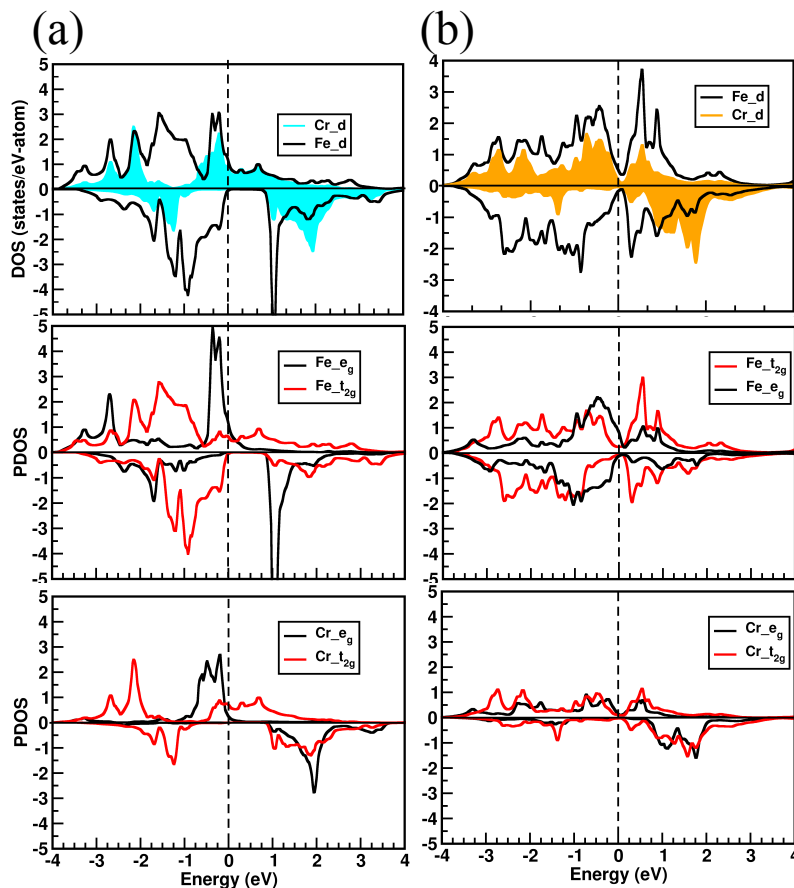


Figure 5. Atom and orbital projected DOS (PDOS) of Fe_2CrTe : (a) cubic, (b) tetragonal Phase, respectively. The e_g states have $d_{x^2-y^2}$ and d_{z^2} orbital contributions and the t_{2g} states have d_{xy} , d_{xz} and d_{yz} orbital contributions.

Table III. Calculated values of total and atom-projected moments (in μ_B) for both the cubic and tetragonal phases.

Phase		$\mu_T/\text{\AA.u.}$	μ_{Fe}	μ_{Cr}	μ_{Te}
Cubic	GGA	3.99	0.89	2.22	-0.003
Tetragonal	GGA	1.99	-0.23	2.31	0.004

the total magnetic moment of the system significantly reduces in the tetragonal phase. This happens due to the change in the partial magnetic moment of the Fe atom. From an overall ferromagnetic coupling observed in the cubic phase, due to the negative moment of Fe, the system assumes an overall ferrimagnetic configuration in the tetragonal phase. The partial moment of the Cr atom remains quite similar in both the cubic and non-cubic cases. The spin-polarized DOS of the d states of the Fe and Cr atom (Figure 5) give clear indication of these. To explore this in more detail, in Figure 7, we plot the total and partial magnetic moments of both the atoms, as a function of c/a values. It is observed that at about c/a of ~ 1.15 , a transition is observed for both the total and partial atomic moments. While the partial moment value of Fe goes from positive ($\sim 1 \mu_B$) to a nega-

tive value ($-0.23 \mu_B$), partial moment of Cr atom make a transition of value of about 2.1 to close to $2.4 \mu_B$. Hence, it is clear that though Cr is the main moment-carrying atom in both the phases, it is the partial moment of Fe atom which leads to a change in magnetic configuration of the system. Additionally, it appears that such a transition of magnetic configuration from ferromagnetic in the cubic phase to ferrimagnetic in the tetragonal phase is independent of the Hubbard U parameter used in this study (Figure S4).⁵⁷

In order to understand the drastic change in the magnetic properties at a particular value of c/a , in Figure 8, we plot the spin-polarized DOS for different c/a values around the value of $c/a = 1.15$. We find that the Cr atom projected DOS (PDOS) is less affected than the Fe PDOS (Figure 8 (a)). But the overall intensity of the minority

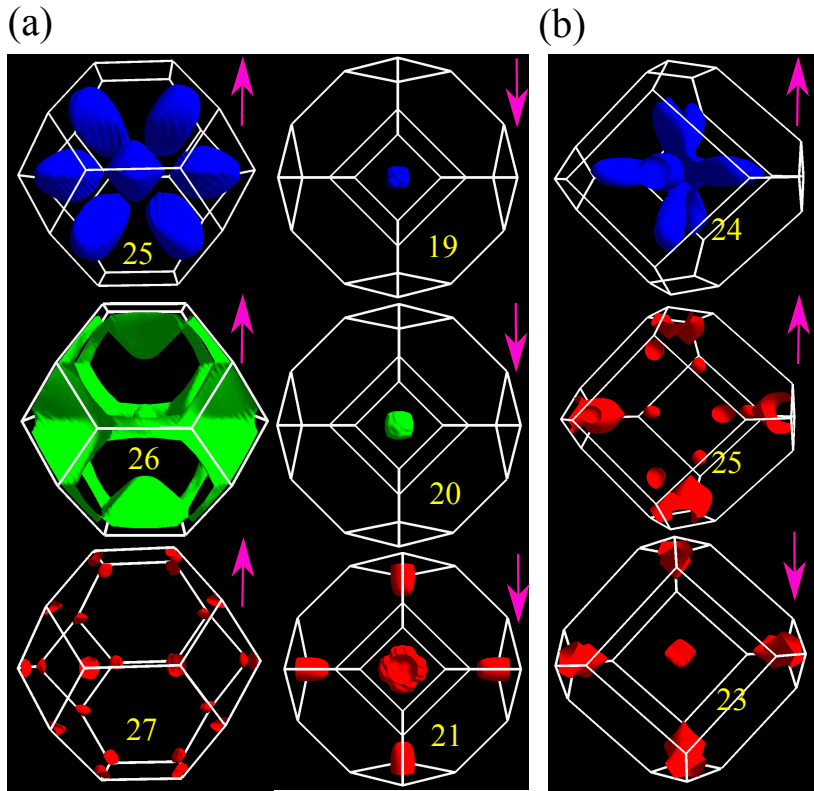


Figure 6. Spin-polarized Fermi surface of Fe_2CrTe : (a) and (b) panels correspond to the cubic and tetragonal phases, respectively. The \uparrow and \downarrow represent Fermi surface due to majority and minority electrons, respectively. We have also mentioned the band index of the bands crossing the E_F , which constitute the Fermi surfaces and those particular bands are shown in Figures S6 and S7⁵⁷ for the cubic and tetragonal phase, respectively.

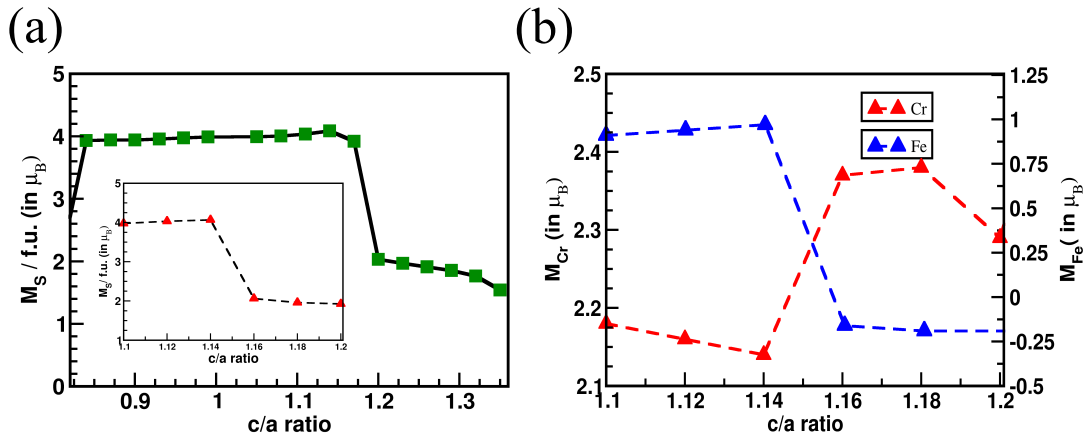


Figure 7. (a) and (b) exhibit variation of total and partial magnetic moments, respectively, plotted as a function of c/a .

spin DOS for Fe seems to have increased. Further, we have observed strong hybridization between the majority spin states of Fe and Cr d electrons near E_F (-0.50 to 0 eV) for the c/a values 1.12 and 1.14, which is absent for the c/a values beyond ~ 1.15 (Figure 8(a)). This might give rise to the difference in Fe and Cr spin moments below and above $c/a = 1.15$. In Figure 8(b), we have

shown the DOS of the Fe-d states for different c/a values near the E_F . The peak around ~ -0.10 eV in the majority DOS is shifted to ~ 0.10 eV as we increase the c/a ratio. Further the peak around ~ -1 eV in the majority DOS is also pushed to the higher energy (*i.e.* towards E_F) as c/a ratio changes from 1.12, 1.14 to 1.16 and 1.18. On the contrary in the minority spin states, we see the trend

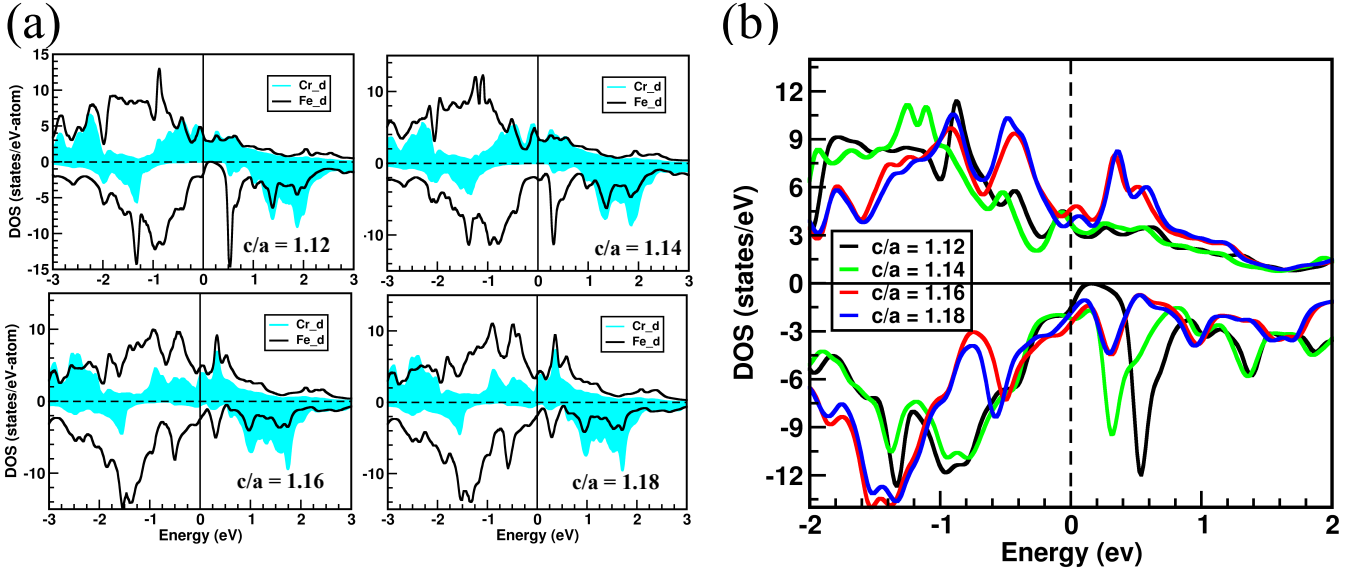


Figure 8. Spin-polarized density of states for tetragonal distortion in Fe₂CrTe for different c/a values. (a) presents orbital projected density of states for both the Cr and Fe atoms and (b) shows the DOS of d orbitals of the Fe atoms corresponding to minority and majority electrons, respectively.

is quite opposite. The minority DOS (around ~ 0.5 eV and -1 eV) are pushed from the lower binding energy to the occupied side with increasing c/a ratio. This is also corroborates well with decrease in exchange-splitting energy of the Fe atoms from 0.91 eV to 0.07 eV as c/a ratio changes from 1.14 to 1.16. On the other hand for the Cr atom the change in the exchange-splitting energy is rather small (1.88 eV and 1.82 eV for c/a ratio 1.14 and 1.16 respectively). The exchange-splitting energy is obtained by calculating the d-band centers of the atoms using VASPKIT programme⁶².

III.1.4. Effect of Isotropic Strain on the Electronic, Magnetic and Elastic Properties of Cubic Fe₂CrTe

It is well-known that, any change in the geometrical properties of Heusler alloy system may affect its electronic, magnetic and mechanical properties^{63–65}. Hence, it is important to probe the effect of lattice constant variation on the electronic structure and magnetic properties of the bulk material. One of the simplest ways is to apply an external pressure or equivalently apply a uniform strain in the system. In our case, we have investigated the electronic, magnetic properties and mechanical stability of the system by applying a uniform strain of $\pm 5\%$ (changing pressure from -20 GPa to 20 GPa). In Figure 9, we have shown these effects. The total magnetic moment of the system remains nearly integer ($\approx 3.99 \mu_B$), almost over the entire range of lattice constants (5.71 - 6.10 Å) and after that the total magnetic moment suddenly increases at 6.22 Å and thereafter decreases (Figure 9(a)). Further, we do not

observe any magnetic phase transition (ferromagnetic to anti-ferromagnetic) over the studied range of lattice constant. Since the cubic phase of Fe₂CrTe shows high spin polarization, we have also verified its HM property under uniform strain (Figure 9(b)) and found that it shows close to 100 % SP at E_F on applying a negative uniform strain in the system. We further study the mechanical stability of the system, when the lattice constant changes. Under uniform pressure (P), the elastic constants are modified according to the following equation⁶³:

$$B_{11} = C_{11} - P ; B_{12} = C_{11} + P ; B_{44} = C_{44} - P$$

and the stability criteria changes to:

$$B_{11} - B_{12} > 0 ; B_{11} + 2B_{12} > 0 ; B_{44} > 0$$

In Figure 9(c), we have shown the change of elastic constants with the lattice constant under uniform strain. The compound is found to be mechanically stable over almost the whole range of lattice constants studied, as it satisfies the stability criteria as discussed above. However, when the lattice constant is too large (~ 6.25 Å), the compound is no longer mechanically stable. This is due to the fact that with increasing lattice constant, the interaction between the atoms weakens and the stability is thus destroyed.

III.2. Fe₂CrTe on MgO Surface

From our previous discussion, we have established that the cubic phase of Fe₂CrTe behaves like a nearly HM sys-

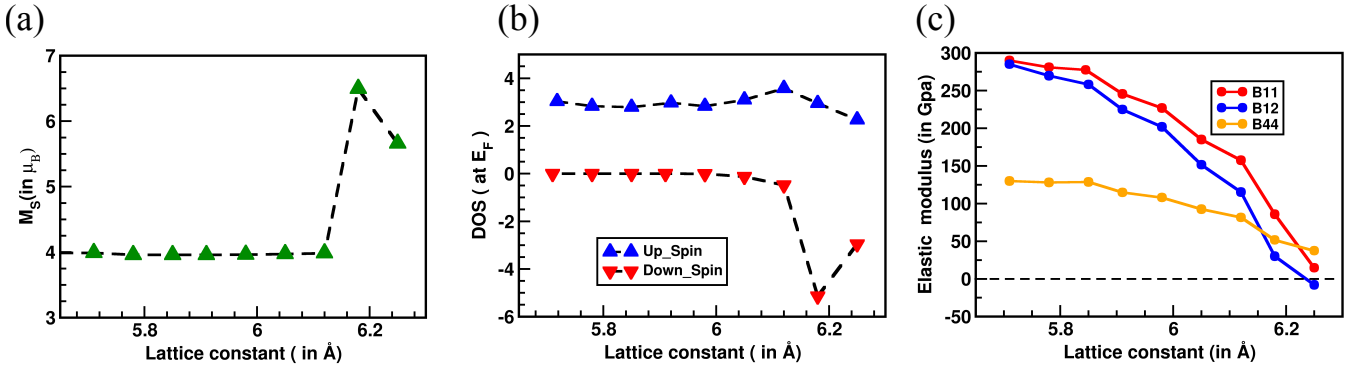


Figure 9. Effect of strain (isotropic pressure) on the (a) magnetic properties; (b) electronic properties; (c) elastic properties of Fe₂CrTe in the cubic phase.

tem. But in reality, HM properties can be highly affected by any kind of crystal disorders; such as defects, surfaces and interfaces. The study of a HM system on a substrate and corresponding surface and interface-related effects on its electronic and magnetic properties can lead to interesting results. In order to simulate an interface, we have constructed the Fe₂CrTe/MgO(001) system (Figure S8)⁵⁷, by placing the O atoms (a) on top of the Cr and Te atoms *i.e.* on a Cr-Te terminated interface and (b) on top of the Fe atoms of a Fe-Fe terminated interface. The Cr-Te terminated interface is found to be energetically more stable. This corroborates well with previous studies on Heusler alloy and MgO based heterojunctions^{4,66,67}, where it has already been reported that YZ interface of X₂YZ FHA, where Y and Z atoms are situated on the top of O atoms, is the most stable one. Hence we consider this interface for further studies. Here we have considered 13 mono-layers (ML) of Fe₂CrTe and 7 ML of MgO with *sim*15 Å of vacuum to prevent interaction between the adjacent surfaces in a periodic arrangement. Further, the in-plane lattice constant of the Fe₂CrTe/MgO surface, was fixed at 4.21 Å ($\frac{a}{\sqrt{2}}$, a being the lattice constant of bulk Fe₂CrTe) in the cubic phase, which has an excellent lattice matching with bulk MgO (4.21 Å).

First we discuss the stability of this interface in the *ab-initio* DFT framework. We have calculated the binding energy and also the surface free energy (γ)⁶⁸, which is defined as,

$$\gamma = \frac{G(T, P_i) - \sum_i n_i \mu_i}{2A}$$

where, G is the Gibbs free energy of the surface, n_i and μ_i are the number and chemical potential of the i^{th} element and A is the surface area of the supercell. The binding energy and surface free energy (γ) are ~ -4.3767 eV/atom and -1.9781 eV/Å², respectively and these indicate a stable composite system. From Table IV, we see that there is some buckling in the interface and sub-surface Cr-Te layers, where the Te atoms move towards the substrate (MgO) side due to higher electronegativity

of Te as compared to Cr. The increase of magnetic moments of the interface atoms (Table IV) is a well-known phenomenon^{69,70}, when the lower hybridization at the surface leads to the enhancement in exchange-splitting of the interface atoms. This can also be confirmed from the atom projected spin-polarized DOS (Figure 10), where we see the majority (minority) spin states of the Cr atoms shift towards higher (lower) binding energy with respect to E_F , as compared to bulk Cr. It is also evident from Figure 10, that the interface states of the minority spin channel are mostly localized at the Fe atoms of the sub-surface layer. As a result, the SP of the surface is significantly reduced as compared to bulk. However, the surface effect is able to penetrate a few ML and rest of the layers show bulk-like properties (as is evident from Table IV and Figure 10).

III.3. Spin-Transport Properties of Fe₂CrTe/MgO/Fe₂CrTe Heterojunction

From our previous discussion, we predict that the Fe₂CrTe cubic alloy may be grown on MgO(001) substrate as it forms an energetically stable surface. In bulk Fe₂CrTe the half-metallic behavior is affected due to the highly dispersive bands in the minority spin channel due to the dominant contribution from the Fe atoms (Figure 3), which is also evident from the non-integer spin magnetic moment ($\sim 4 \mu_B$). Thus transport in both the spin channels is expected in case of cubic phase of Fe₂CrTe. Further, the SP at E_F for the tetragonal phase has been found to be much less than that of the cubic phase. However, we find a significantly strong SP of transport even at high temperature, when we calculate the temperature dependence of the spin-polarized conductivity (Figure S9)⁵⁷, specially in the cubic phase. This indicates even though Fe₂CrTe may not completely be half-metallic, it may be a useful for a spin-injector material even at higher temperature.

MTJ materials with an electrode with a reasonably

Table IV. Calculated electronic, geometric and magnetic properties of Fe₂CrTe/MgO interface. Surface buckling (δl in Å), atomic magnetic moments (in μ_B) and the SP (in %) at E_F are shown in the table. Bulk values are also given for comparison.

Atomic Layer	δl	SP	Atomic Magnetic Moments		
			Cr	Fe	Te
Interface (S)	0.21	71	3.12	–	-0.05
S-1	0.00	11	–	1.82	–
S-2	0.20	94	2.05	–	-0.07
S-3	0.00	41	–	0.98	–
S-4	0.00	94	2.10	–	-0.05
Bulk	–	95	2.22	0.89	-0.04

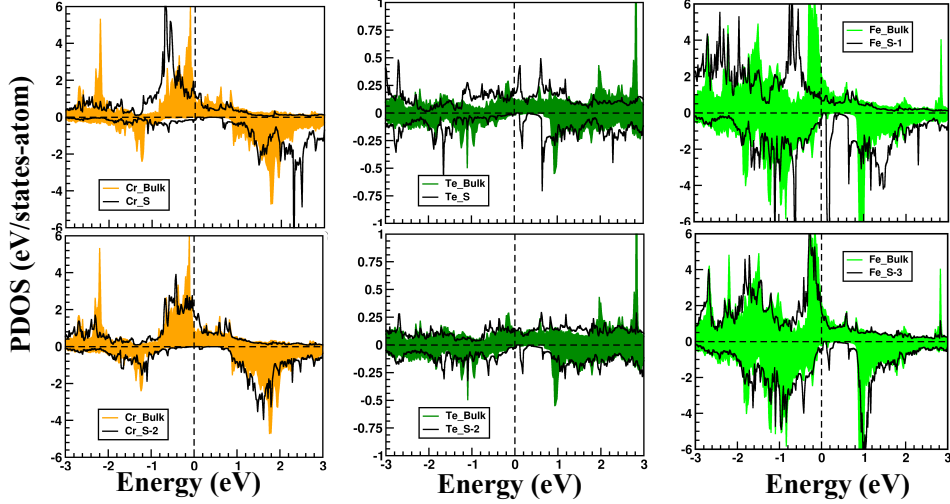


Figure 10. The spin-polarized, atom projected density of states are shown for atoms at different layers for the composite system with Cr-Te/MgO interface. Here S, S-1, S-2, and S-3 represent surface and subsurface layers as we go away from the interface, respectively.

high SP at E_F have recently gained lots of attention, due to their high TMR ratio, where the resulting current in the junction strongly depends on the relative magnetization of the electrode.^{3,4} Here we investigate the Fe₂CrTe/MgO/Fe₂CrTe heterojunction to explore its MTJ properties, in both the phases. It may be noted that the tetragonal phase of Fe₂CrTe exhibits a lattice mismatch of 7% with MgO (in-plane lattice constant = $a/\sqrt{2}$). Here we have constructed our heterojunction with 13 ML of Fe₂CrTe and have taken 5 ML of MgO. In Table V, we have shown the transmittance value and TMR ratio of the heterojunction for cubic and tetragonal phases of Fe₂CrTe, where the TMR value is defined as $\frac{G_{PC}-G_{APC}}{G_{APC}}$, where G_{PC} and G_{APC} indicate the total conductance for the MTJs in the parallel (PC) and anti-parallel (APC) state. Despite the fact that the cubic phase has a higher SP value, the TMR ratio indicates a 10 fold rise in the TMR ratio value for the tetragonal phase compared to the cubic phase (Table V). To understand this, we examine the majority spin band structure of both the phases along the $\langle 001 \rangle$ direction (Figure 3

and Figure 4). It has already been established that the Δ_1 band in the majority spin state is essential to obtain a large TMR ratio for MgO-based MTJs.^{3,71} We see that the bands with Δ_1 symmetry along the $\langle 001 \rangle$ direction are only present for the tetragonal phase. Here we must keep in mind the possibility that these theoretical values can be constrained by the presence of a variety of disorders and defects at the interface that may develop during the sample growth. Therefore, our predicted values of the TMR ratio define the upper limit of the same.

For a comprehensive understanding of the above spin-dependent conductance and TMR effect, in Figure 11 we show the k-resolved transport properties at the E_F of the heterojunction with MgO (with layer thickness of 5 ML) in PC and APC state for the cubic phase of Fe₂CrTe. The majority spin transmission in PC state is found to be negligible around the center of the BZ, though MgO has a small decay constant (κ) around Γ point, as can be seen from the complex band structure of MgO (Figure S10).⁵⁷ It is evident from the orbital projected majority spin band structure of bulk Fe₂CrTe that there are no in-

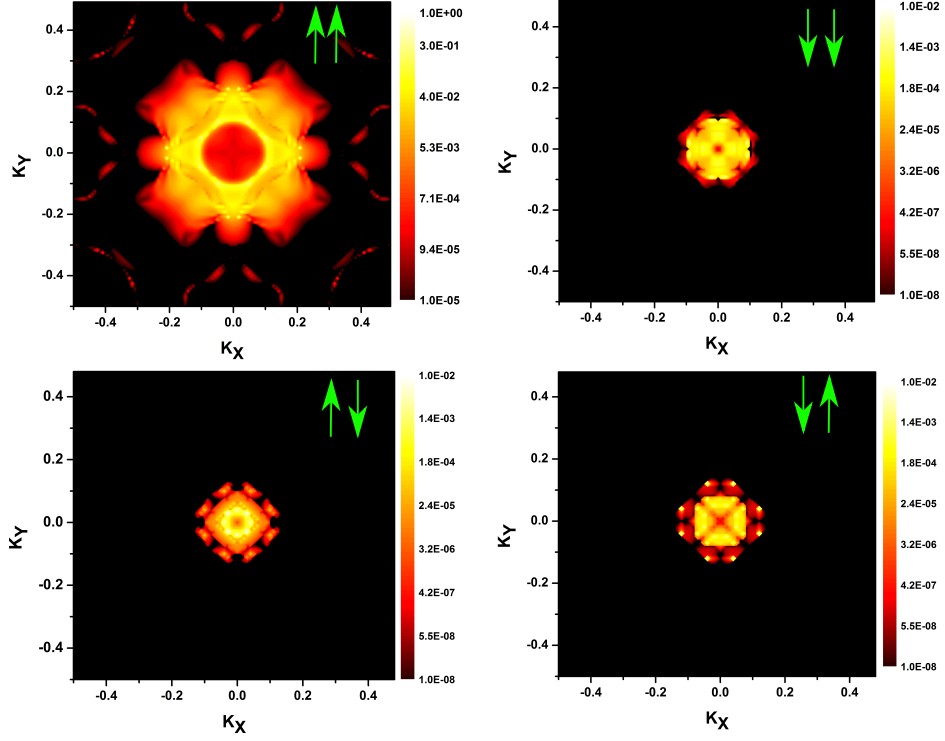


Figure 11. K-resolved Transmittance in parallel magnetization case for $\text{Fe}_2\text{CrTe}/\text{MgO}/\text{Fe}_2\text{CrTe}$ heterojunction with Cr-Te interface for 5 ML of with cubic phase of Fe_2CrTe : Top and bottom panels are for parallel (PC) and anti-parallel spin configurations (APC), respectively.

Table V. Calculated transport properties of $\text{Fe}_2\text{CrTe}/\text{MgO}/\text{Fe}_2\text{CrTe}$ junctions for the cubic and tetragonal phases. $G_{PC}^{\uparrow\uparrow}$ ($G_{PC}^{\downarrow\downarrow}$) are spin-up (spin-down) conductance at the Fermi energy for parallel (P) spin configuration. $G_{PC}^{\uparrow\downarrow}$ ($G_{PC}^{\downarrow\uparrow}$) are the spin up-to-spin down and spin down-to-spin up conductance in the anti-parallel configuration state (APC), respectively. The tunnel magnetoresistance ratio is defined as $\frac{G_{PC}-G_{APC}}{G_{APC}}$, where $GP = G_{PC}^{\uparrow\uparrow} + G_{PC}^{\downarrow\downarrow}$ and $G_{APC} = G_{APC}^{\uparrow\downarrow} + G_{APC}^{\downarrow\uparrow}$.

Phase	Layer thickness	$G_{PC}^{\uparrow\uparrow}$	$G_{PC}^{\downarrow\downarrow}$	$G_{APC}^{\uparrow\downarrow}$	$G_{APC}^{\downarrow\uparrow}$	TMR (%)
Cubic	5	3.567×10^{-3}	5.342×10^{-6}	6.678×10^{-6}	5.372×10^{-6}	300
Tetragonal	5	7.050×10^{-3}	4.461×10^{-5}	3.048×10^{-7}	1.716×10^{-6}	3522

coming majority-spin Δ_1 states at the E_F (Figure 3). In contrast, for the minority spin channel in the PC state, we observe tunneling hot-spots around Γ point, however showing a much weaker transmission. Apart from the highly conducting channel around the Γ point, we observe appearance of conducting channels around the Brillouin zone corners for the majority spin channel showing a four-fold rotational symmetry of the Fe_2CrTe electrode. These are identified as resonant tunneling states.^{3,71} In the APC state the spin up and down channels exhibit similar transmission properties with considerably large tunneling states around the Γ point (Figure 11).

Now as we increase the barrier thickness the transmission around Γ point gets highly affected for the majority spin channel, showing astonishingly small transmission around Γ and the resonant tunneling states are

also diminished. However, transmission for the minority states are not largely affected with increasing barrier thickness (Figure S10).⁵⁷ This large decrement in the majority spin transmission can be explained from the majority spin band structure of the bulk cubic Fe_2CrTe (Figure 3), where we do not observe any bands crossing the E_F along the Γ - X direction (*i.e.* along the propagation direction (001)). These bands are mainly responsible for the highly spin-polarized transmission^{3,4,71}, provided that those bands have some preferred orbital character. Due to the absence of such bands along the Γ -X direction in the majority spin channel, we observe large decrement in the majority spin transmission with increasing barrier thickness (Table V and Figure S10⁵⁷).

To understand why larger TMR ratio is possible for the tetragonal phase as compared to the cubic phase,

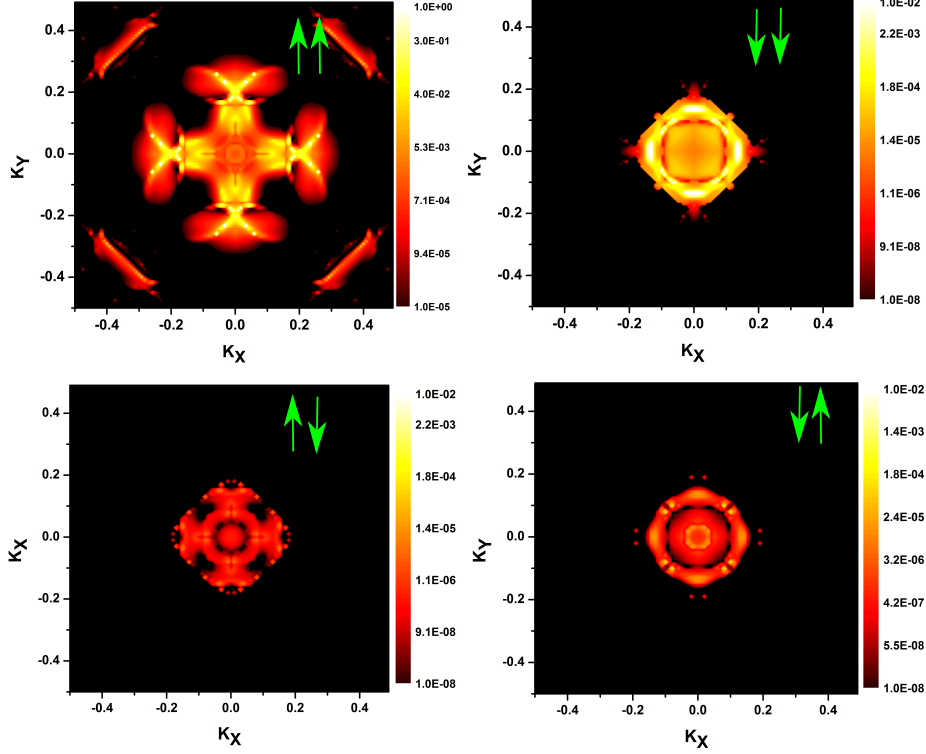


Figure 12. K-resolved Transmittance in parallel magnetization case for $\text{Fe}_2\text{CrTe}/\text{MgO}/\text{Fe}_2\text{CrTe}$ heterojunction with Cr-Te interface for 5 ML of MgO and with tetragonal phase of Fe_2CrTe : Top and bottom panels are for parallel (PC) and anti-parallel spin configurations (APC), respectively.

we further investigate the microscopic tunneling process for the tetragonal phase. In Figure 12, we have plotted the spin- and k -resolved transmission coefficients at E_F , $T^\sigma(E_F, K_{||})$ for the tetragonal Fe_2CrTe phase in both PC and APC states. This provides a vivid picture of how tunneling process can be realized in this heterojunction. At a first glance, all the transmission patterns (including parallel and anti-parallel) have a four-fold rotational symmetry, which is in accordance with the C_{4v} symmetry of the MTJ heterostructure. We note that for the majority spin electrons in the PC state, the very sharp transmission features around the Γ point dominate the transmission process. However, minority spin electrons in the PC state show Γ -centric transmission, which are of much weaker intensity. We observe for the tetragonal phase that there is an overall increase in the transmission of the majority as well as of the minority spins around the Γ point in the parallel configuration, as compared to the cubic phase. This is primarily due to the presence of Δ_1 symmetric bands in the bulk tetragonal phase, along the $\langle 001 \rangle$ direction. In the APC state, however, we find that there is a dramatic reduction in the transmission of both the spin channels (Figure 12), due to a stronger suppression of the electron tunneling process, which leads to the larger TMR ratio for the tetragonal phase as compared to the cubic phase.

IV. CONCLUSION

In this work, we have carried out a first principles study on the structural, mechanical, electronic and transport properties of a novel full Heusler chalcogenide, Fe_2CrTe . The compound is found to undergo a volume conserving tetragonal distortion and a clear minimum has been observed at $c/a \sim 1.26$. The cubic phase shows a ferromagnetic behavior with a nearly half metallic character, whereas the tetragonal phase exhibits a ferrimagnetic and fully metallic nature. This behavior has been found to be robust against a sizable value of Hubbard onsite electron-electron correlation term for both the transition metal atoms. The compound is found to possess no negative phonon frequencies in both the phases and no martensite phase transition (MPT) was observed, as suggested from the temperature dependent free energy behavior. Further we have also established the mechanical stability of both the phases. We have also studied the effect of uniform strain on the electronic and mechanical properties of the system in cubic phase. It shows 100% SP on applying a negative uniform strain and the compound is found to be mechanically stable over almost the whole range of lattice constant. To probe the effect of substrate on various physical properties a thin film of 13 mono-layers of Fe_2CrTe is placed on a MgO substrate, which shows

an energetically stable composite system and the spin polarization has been found to continue to be high for the cubic phase (above 70%). We have further investigated the transmission profile of Fe₂CrTe/MgO/Fe₂CrTe heterojunction in both the cubic and tetragonal phases. Spin-transport properties for the tetragonal phase looks promising for lower thickness of spacer layer (5 ML). Finally, in light of all the above discussions, synthesis and characterization of the predicted alloy seem essential to understand its structural, electronic, magnetic and spin transport properties and our present work awaits the ex-

perimental validation.

V. ACKNOWLEDGEMENTS

Authors thank the director, RRCAT for facilities and encouragement. We thank A. Banerjee, H. Ghosh and T. Ganguli for scientific discussions. The scientific computing group, computer division of RRCAT, Indore is thanked for the help in installing and support in smooth running of the codes. JB thanks D. Pandey, A. Kumar for useful discussions during the work. JB and RD thank RRCAT and HBNI for financial support.

-
- ¹ R. A. de Groot, F. M. Mueller, P. G. v. Engen, and K. H. J. Buschow, *Phys. Rev. Lett.* **50**, 2024 (1983).
- ² P. Webster, *J. Phys. Chem. Solids* **32**, 1221 (1971).
- ³ Y. Miura, H. Uchida, Y. Oba, K. Abe, and M. Shirai, *Phys. Rev. B* **78**, 064416 (2008).
- ⁴ B. Hülsen, M. Scheffler, and P. Kratzer, *Phys. Rev. Lett.* **103**, 046802 (2009).
- ⁵ T. Roy, D. Pandey, and A. Chakrabarti, *Phys. Rev. B* **93**, 184102 (2016).
- ⁶ Enamullah and S.-C. Lee, *J. Alloys Compd.* **765**, 1055 (2018).
- ⁷ M. Baral and A. Chakrabarti, *Phys. Rev. B* **99**, 205136 (2019).
- ⁸ X.-H. Kang and J.-M. Zhang, *J. Phys. Chem. Solids* **105**, 9 (2017).
- ⁹ N. Kervan and S. Kervan, *J. Phys. Chem. Solids* **72**, 1358 (2011).
- ¹⁰ X. Zhu, Y. Wang, L. Wang, Y. Dai, and C. Luo, *J. Phys. Chem. Solids* **75**, 391 (2014).
- ¹¹ J. C. Slater, *Phys. Rev.* **49**, 931 (1936).
- ¹² L. Pauling, *Phys. Rev.* **54**, 899 (1938).
- ¹³ I. Galanakis, P. H. Dederichs, and N. Papanikolaou, *Phys. Rev. B* **66**, 174429 (2002).
- ¹⁴ H. Z. Luo, H. W. Zhang, Z. Y. Zhu, L. Ma, S. F. Xu, G. H. Wu, X. X. Zhu, C. B. Jiang, and H. B. Xu, *J. Appl. Phys.* **103**, 083908 (2008).
- ¹⁵ A. Hirohata, J. Sagar, L. Lari, L. R. Fleet, and V. K. Lazarov, *Appl. Phys. A* **111**, 423 (2013).
- ¹⁶ K. Elphick, W. Frost, M. Samiepour, T. Kubota, K. Takahashi, H. Sukegawa, S. Mitani, and A. Hirohata, *Sci. Technol. Adv. Mater.* **22**, 235 (2021).
- ¹⁷ L. Bainsla and K. G. Suresh, *Appl. Phys. Rev.* **3**, 031101 (2016).
- ¹⁸ R. Dutt, J. Bhattacharya, and A. Chakrabarti, *J. Phys. Chem. Solids* **167**, 110704 (2022).
- ¹⁹ D. Pandey and A. Chakrabarti, *Physics Letters A* **383**, 2914 (2019).
- ²⁰ D. Pandey, R. Gangwar, J. Bhattacharya, and A. Chakrabarti, *Surface Science* **714**, 121910 (2021).
- ²¹ N. Ru and I. R. Fisher, *Phys. Rev. B* **73**, 033101 (2006).
- ²² X.-G. Zhu, Y. Zhang, W. Feng, B.-K. Yuan, Q. Liu, R.-Z. Qiu, D.-H. Xie, S.-Y. Tan, Y. Duan, Y. Fang, W. Zhang, and X.-C. Lai, *New Journal of Physics* **18**, 093015 (2016).
- ²³ A. Chakrabarti, M. Siewert, T. Roy, K. Mondal, A. Banerjee, M. E. Gruner, and P. Entel, *Phys. Rev. B* **88**, 174116 (2013).
- ²⁴ S. R. Barman, S. Banik, and A. Chakrabarti, *Phys. Rev. B* **72**, 184410 (2005).
- ²⁵ R. Ducher, R. Kainuma, and K. Ishida, *J. Alloys Compd.* **463**, 213 (2008).
- ²⁶ M. Siewert, M. E. Gruner, A. Dannenberg, A. Chakrabarti, H. C. Herper, M. Wuttig, S. R. Barman, S. Singh, A. Al-Zubi, T. Hickel, J. Neugebauer, M. Gillessen, R. Dronskowski, and P. Entel, *Appl. Phys. Lett.* **99**, 191904 (2011).
- ²⁷ T. Roy and A. Chakrabarti, *J. Magn. Magn. Mater.* **401**, 929 (2016).
- ²⁸ Y. Feng, H. Ding, X. Li, B. Wu, and H. Chen, *Journal of Applied Physics* **131**, 133901 (2022), <https://doi.org/10.1063/5.0081588>.
- ²⁹ Z. Cui, H. Ding, and Y. Feng, *Phys. Chem. Chem. Phys.* **23**, 17984 (2021).
- ³⁰ Y. Miura, K. Abe, and M. Shirai, *Phys. Rev. B* **83**, 214411 (2011).
- ³¹ H. Han, T. Feng, L. Fan, Z. Zhao, M. Li, and K. Yao, *J. Magn. Magn. Mater.* **438**, 95 (2017).
- ³² Z. Gercsi, A. Rajanikanth, Y. K. Takahashi, K. Hono, M. Kikuchi, N. Tezuka, and K. Inomata, *Appl. Phys. Lett.* **89**, 082512 (2006).
- ³³ T. Roy, M. Tsujikawa, T. Kanemura, and M. Shirai, *J. Magn. Magn. Mater.* **498**, 166092 (2020).
- ³⁴ G. Kresse and J. Furthmüller, *Phys. Rev. B* **54**, 11169 (1996).
- ³⁵ G. Kresse and D. Joubert, *Phys. Rev. B* **59**, 1758 (1999).
- ³⁶ J. P. Perdew, K. Burke, and M. Ernzerhof, *Phys. Rev. Lett.* **77**, 3865 (1996).
- ³⁷ A. Marmier, Z. A. Lethbridge, R. I. Walton, C. W. Smith, S. C. Parker, and K. E. Evans, *Computer Physics Communications* **181**, 2102 (2010).
- ³⁸ A. Smogunov, A. Dal Corso, and E. Tosatti, *Phys. Rev. B* **70**, 045417 (2004).
- ³⁹ S. Baroni, S. de Gironcoli, A. Dal Corso, and P. Giannozzi, *Rev. Mod. Phys.* **73**, 515 (2001).
- ⁴⁰ H. Joon Choi and J. Ihm, *Phys. Rev. B* **59**, 2267 (1999).
- ⁴¹ S. Karki, V. Rogers, P. Jadaun, D. S. Marshall, and J. A. C. Inorvia, *Adv. Theory Simul.* **4**, 2100309 (2021).
- ⁴² P. Blaha, K. Schwarz, G. K. H. Madsen, D. F. Kvasnicka, J. Luitz, R. Laskowski, F. Tran, and L. D. Marks (2019).
- ⁴³ M. Siewert, M. E. Gruner, A. Dannenberg, A. Hucht, S. M. Shapiro, G. Xu, D. L. Schlagel, T. A. Lograsso, and P. En-

- tel, Phys. Rev. B **82**, 064420 (2010).
- ⁴⁴ A. Togo and I. Tanaka, Scr. Mater. **108**, 1 (2015).
- ⁴⁵ S. Paul, B. Sanyal, and S. Ghosh, J. Phys. Condens. Matter **27**, 035401 (2014).
- ⁴⁶ A. T. Zayak, P. Entel, K. M. Rabe, W. A. Adeagbo, and M. Acet, Phys. Rev. B **72**, 054113 (2005).
- ⁴⁷ T. Roy, M. E. Gruner, P. Entel, and A. Chakrabarti, J. Alloys Compd. **632**, 822 (2015).
- ⁴⁸ R. Hill, Proceedings of the Physical Society. Section A **65**, 349 (1952).
- ⁴⁹ W. Zhi-jian, E.-j. Zhao, H.-p. Xiang, X.-f. Hao, X.-j. Liu, and J. Meng, Phys. Rev. B **76**, 054115 (2007).
- ⁵⁰ S. Ozdemir Kart and T. Cagin, J. Alloys Compd. **508**, 177 (2010).
- ⁵¹ T. Kanomata, Y. Chieda, K. Endo, H. Okada, M. Nagasako, K. Kobayashi, R. Kainuma, R. Y. Umetsu, H. Takahashi, Y. Furutani, H. Nishihara, K. Abe, Y. Miura, and M. Shirai, Phys. Rev. B **82**, 144415 (2010).
- ⁵² X. Luan, H. Qin, F. Liu, Z. Dai, Y. Yi, and Q. Li, Crystals **8** (2018).
- ⁵³ S. Pugh, The London, Edinburgh, and Dublin Philosophical Magazine and Journal of Science **45**, 828 (1954).
- ⁵⁴ D. G. Pettifor, Mater. Sci. Technol. **8**, 345 (1992).
- ⁵⁵ M. I. Naher and S. H. Naqib, Scientific Reports **11**, 5592 (2021).
- ⁵⁶ Y. Han, Y. Wu, T. Li, R. Khenata, T. Yang, and X. Wang, Materials **11** (2018), 10.3390/ma11050797.
- ⁵⁷ J. Bhattacharya and A. Chakrabarti, Supplementary Information.
- ⁵⁸ S. L. Dudarev, G. A. Botton, S. Y. Savrasov, C. J. Humphreys, and A. P. Sutton, Phys. Rev. B **57**, 1505 (1998).
- ⁵⁹ B. N. Cox, M. A. Coulthard, and P. Lloyd, Journal of Physics F: Metal Physics **4**, 807 (1974).
- ⁶⁰ R. Paudel, G. C. Kaphle, M. Batouche, and J. Zhu, International Journal of Quantum Chemistry **120**, e26417 (2020), <https://onlinelibrary.wiley.com/doi/pdf/10.1002/qua.26417>.
- ⁶¹ A. Chakrabarti, S. D'Souza, and S. Barman, Physica B: Condensed Matter **407**, 3547 (2012).
- ⁶² V. Wang, N. Xu, J.-C. Liu, G. Tang, and W.-T. Geng, Computer Physics Communications **267**, 108033 (2021).
- ⁶³ C. Zhang, H. Huang, C. Wu, Z. Zhu, Z. He, and G. Liu, Frontiers in Physics **8** (2020).
- ⁶⁴ M. Singh, H. S. Saini, J. Thakur, A. H. Reshak, and M. K. Kashyap, Journal of Alloys and Compounds **580**, 201 (2013).
- ⁶⁵ R. B. Ray, G. C. Kaphle, R. K. Rai, D. K. Yadav, R. Paudel, and D. Paudyal, Journal of Alloys and Compounds **867**, 158906 (2021).
- ⁶⁶ Y. Miura, H. Uchida, Y. Oba, K. Abe, and M. Shirai, Phys. Rev. B **78**, 064416 (2008).
- ⁶⁷ M. Yamamoto, D. Asakura, T. Koide, Y. Miura, and M. Shirai, Phys. Rev. B **81**, 144417 (2010).
- ⁶⁸ S. Zarei, S. J. Hashemifar, H. Akbarzadeh, and Z. Hafari, J. Phys. Condens. Matter **21**, 055002 (2008).
- ⁶⁹ J. Bhattacharya, D. Pandey, S. R. Barman, and A. Chakrabarti, J. Magn. Magn. Mater. **540**, 168398 (2021).
- ⁷⁰ P. Habibi, C. Barreteau, and A. Smogunov, J. Phys. Condens. Matter **25**, 146002 (2013).
- ⁷¹ W. H. Butler, Sci. Technol. Adv. Mater. **9**, 014106 (2008).